The Astrophysical Journal, 886:70 (16pp), 2019 November 20 https://doi.org/10.3847/1538-4357/ab4e94

An Empirical Model of Energetic Neutral Atom Imaging of the Heliosphere and Its Implications for Future Heliospheric Missions at Great Heliocentric Distances

A. Galli[1], P. Wurz[1], H. Fichtner[2], Y. Futaana[3], and S. Barabash[3]
[1] Physics Institute, University of Bern, Bern, Switzerland; andre.galli@space.unibe.ch
[2] Ruhr University, Bochum, Germany
[3] IRF Swedish Institute of Space Physics, Kiruna, Sweden
Received 2019 July 15; revised 2019 October 15; accepted 2019 October 15; published 2019 November 21

Abstract

Several concepts for heliospheric missions operating at heliocentric distances far beyond Earth orbit are currently investigated by the scientific community. The mission concept of the *Interstellar Probe*, e.g., aims at reaching a distance of 1000 au away from the Sun within this century. This would allow the coming generation to obtain a global view of our heliosphere from an outside vantage point by measuring the energetic neutral atoms (ENAs) originating from the various plasma regions. It would also allow for direct sampling of the unperturbed interstellar medium, as well as for many observation opportunities beyond heliospheric science, such as visits to Kuiper Belt objects, a comprehensive view on the interplanetary dust populations, and infrared astronomy free from the foreground emission of the zodiacal cloud. In this study, we present a simple empirical model of ENAs from the heliosphere and derive basic requirements for ENA instrumentation on board a spacecraft at great heliocentric distances. We consider the full energy range of heliospheric ENAs from 10 eV to 100 keV because each part of the energy spectrum has its own merits for heliospheric science. To cover the full ENA energy range, two or three different ENA instruments are needed. Thanks to parallax observations, some insights about the nature of the *IBEX* ribbon and the dimensions of the heliosphere can already be gained by ENA imaging from a few au heliocentric distance. To directly reveal the global shape of the heliosphere, measurements from outside the heliosphere are, of course, the best option.

Unified Astronomy Thesaurus concepts: Heliosphere (711); Heliosheath (710); Astrosphere interstellar medium interactions (106); Space plasmas (1544); Deep space probes (366)

1. Introduction

In this study, we investigate basic requirements for energetic neutral atom (ENA) instruments on a spacecraft headed for heliocentric distances beyond Mars orbit for the ENA energy range between 10 eV and 100 keV. An ENA is produced when an ion of a plasma population exchanges its charge with an ambient neutral atom (Roelof et al. 1985; Gruntman et al. 2001). The resulting ENA leaves its source region on a ballistic trajectory, no longer influenced by electromagnetic fields. This allows an ENA camera to image the ion distribution of remote plasma regions (Wurz 2000; Fahr et al. 2007).

Because of its remote sensing character, ENA imaging is an indispensable method to derive a global view of the heliosphere. The heliosphere is the vast plasma region of the solar wind expanding against the surrounding interstellar medium (ISM). The ISM flows past the heliosphere at roughly 25 km s^{-1} (McComas et al. 2015). This relative flow speed defines an upwind and a downwind direction in the heliosphere. The outer plasma boundary between the solar wind and the ISM is called the heliopause. The two *Voyager* spacecraft have crossed this boundary in the upwind direction at roughly 120 au from the Sun (Stone et al. 2013). The heliosphere itself is divided by the termination shock (Burlaga et al. 2005, 2008) into an inner region of supersonic solar wind and an outer region of shocked solar wind (the inner heliosheath). Our current knowledge or lack thereof of the heliosphere is illustrated by the artist's impression in Figure 1: the shape and dimension of the heliosphere in the downwind hemisphere are unknown (see Section 2.1), and the existence of a bow wave or a bow shock in the ISM approaching the heliopause is still a matter of debate (McComas et al. 2012; Zank et al. 2013; Scherer & Fichtner 2014). Our knowledge about the heliosphere owes a lot to in situ plasma measurements and remote ENA imaging performed at 1 au (see Section 2.5), but some questions about the global heliosphere shape, plasma populations, and pressure balances beyond the termination shock may be impossible to answer with observations restricted to the inner solar system.

A NASA-funded study currently investigates the scientific and technical requirements for an *Interstellar Probe* with the goal of reaching 1000 au within 50 yr. The science targets include exploration of the heliosphere and its interaction with the ISM, characterization of the circumsolar dust disk, exploration of Kuiper Belt objects, and astronomical observations in the infrared wavelength range beyond the zodiacal cloud (McNutt et al. 2018; Brandt et al. 2019). On a similar note, the China National Space Administration is investigating a mission scenario in which two "Heliospheric Boundary Explorers" would be launched toward the upwind and toward the downwind direction of the heliosphere, respectively, to reach 100 au distance by 2049 (Zong 2018). For ESA's Cosmic Vision, the Local Interstellar Medium Observatory (LIMO) was proposed to accurately sample the interstellar neutral (ISN) gas and dust and to measure heliospheric ENAs at 1° angular resolution at a heliocentric distance of 3 au, thus avoiding many complications introduced by solar gravity and radiation closer to the Sun (Barabash et al. 2019).

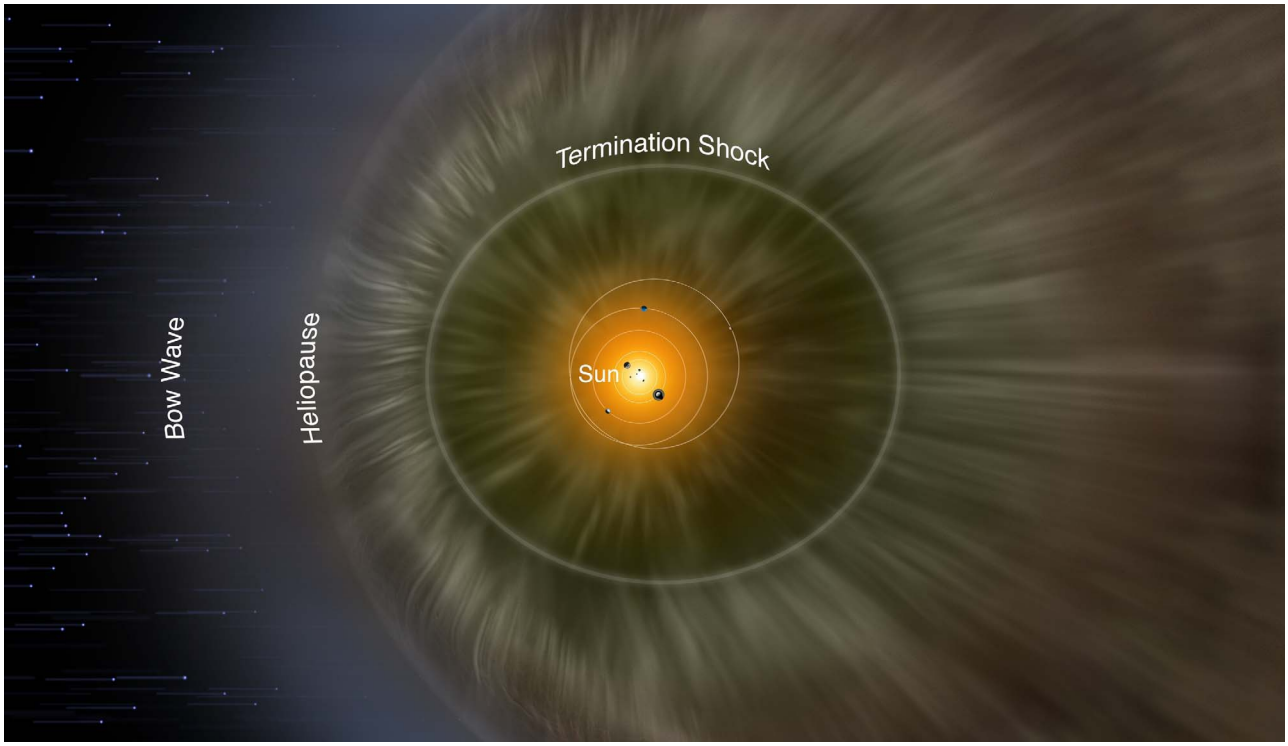

Figure 1. Artist's impression of the heliosphere. Image Credit: *IBEX* Team/Adler Planetarium.

A spacecraft at great heliocentric distance obviously allows for many new ground-breaking measurements in addition to ENA imaging. In this study, we limit ourselves to the prediction and discussion of heliospheric ENAs: we have integrated the existing measurements of heliospheric ENAs from the heliosheath and beyond into a simple empirical model. This allows us to make some predictions for an ENA instrument on board a spacecraft at heliocentric distances beyond Mars orbit. ISN He, H, and other ISN species flowing into the heliosphere (Müller & Zank 2004; Witte 2004; Möbius et al. 2012; Rodríguez Moreno et al. 2012; Saul et al. 2012; Kubiak et al. 2014; McComas et al. 2015; Park et al. 2016; Galli et al. 2019) could also be measured with ENA cameras such as *IBEX*-Lo (Fuselier et al. 2009) or with a mass spectrometer (Barabash et al. 2019). However, we have to relegate questions about ISN observation strategies to a future publication because our heliosphere model currently does not include ISN trajectories. The ISN hydrogen is just modeled as a static density relevant for ENA sources and losses. Measuring ISN will be an important goal for a heliospheric mission bound to heliocentric distances beyond 1 au: the effects of the Sun's gravity, solar wind pressure, and ionization rates drop with the square of the distance to the Sun; thus, ISN measurements at several au or beyond will closely resemble the ISN at the heliopause in terms of energy, direction, and composition. A fast-moving spacecraft ($\geqslant$25 km s^{-1}) must be heading to a vantage point in the upwind hemisphere to seize this opportunity for ISN sampling.

2. The Empirical Model of Heliospheric ENAs

We have created a simple empirical model to predict the differential intensity $j_{\rm ENA}$ (in units of cm^{-2} sr^{-1} s^{-1} keV^{-1}) of heliospheric ENAs an ENA camera would observe for any given location and viewing direction. The fundamental ENA equation,

$$j_{\rm ENA}(E) = \int_{\rm LOS} dl\,(j_p(E) n_{\rm H}\,\sigma(E)) - L(E), \qquad (1)$$

tells us that a hydrogen ENA model requires the local proton intensity $j_p(E)$, neutral densities $n_{\rm H}$, charge-exchange cross sections $\sigma(E)$ for the reaction $H^+ + H \rightarrow H^* + H^+$, and the spatially variable ENA loss term $L(E)$ to predict $j_{\rm ENA}$ for a given line of sight (LOS).

Equation (1) is a simplification for several reasons: most importantly, we only consider hydrogen ENAs here. The second most abundant heliospheric species, helium ENAs from neutralized solar wind and pickup ions, is expected to generate an intensity of typically 1 cm^{-2} sr^{-1} s^{-1} keV^{-1} at 1 au for optimum observation conditions, i.e., 1 keV ENA energy and observing the downwind region (Swaczyna et al. 2017). This He signal is two orders of magnitude weaker than typical H ENA intensities at 1 au and has not been observed yet, but it should be detectable with the future *IMAP*-Hi instrument (Swaczyna et al. 2017; McComas et al. 2018). The long cooling length of keV helium ions in the heliosheath would make He ENAs ideally suited to probe the far heliosheath (Swaczyna et al. 2017).

We also assume that the hydrogen ENAs are moving along straight lines as soon as they have been created. Gravity forces and the influence of solar UV radiation and solar wind are therefore neglected. This is acceptable as long as we consider only ENAs with energies of at least 100 eV or heliocentric distances greater than 1 au. The sum of these effects would change the observed energy of 100 eV ENAs observed at 1 au by less than 10%, and the deflection angle relative to the original trajectory would be at most 1° at 1 au for 100 eV ENAs (and even smaller for higher energies) for any solar wind conditions (Bzowski 2008). For a 20 eV ISN H atom traveling

toward the Sun, deviations from a straight trajectory become notable only for heliocentric distances less than 3 au for any solar conditions (Rahmanifard et al. 2019).

Finally, neutral species other than hydrogen could in principle also neutralize protons. However, helium as the most abundant nonhydrogen species has a density of only $n_{\rm He} \simeq 0.01 \ldots 0.02\,{\rm cm}^{-3}$ everywhere inside and beyond the heliopause (Gloeckler & Geiss 2001; Müller & Zank 2004). This is one order of magnitude less than $n_{\rm H}$. Because the charge-exchange cross section for the reaction $H^+ + He \rightarrow H^* + He^+$ is also at least one order of magnitude smaller than for $H^+ + H \rightarrow H^* + H^+$ at all energies below 10 keV (Barnett 1990; Lindsay & Stebbings 2005), the neutral helium would only have to be considered for ENAs of energies exceeding 100 keV.

In the following, we will present how we implemented the individual terms in Equation (1) and their underlying assumptions in more detail.

2.1. Heliospheric Shapes

First, we must define closed three-dimensional shapes for the termination shock and for the heliopause to decide which local ion populations to consider for the LOS integration in Equation (1). Whether a bow shock forms around the heliopause or not is still debated (McComas et al. 2012; Zank et al. 2013; Scherer & Fichtner 2014), but it is irrelevant for our current model.

Our shape of the termination shock conforms to the observational constraints from *Voyager 1* and *2* (they crossed the termination shock toward the upwind direction at heliocentric distances of 94 and 83 au; Burlaga et al. 2005, 2008) and is consistent with *IBEX* ENA spectra (see Schwadron et al. 2011; Galli et al. 2016; Reisenfeld et al. 2016). We model the termination shock as an ellipsoid whose center is shifted with respect to the Sun:

$$\begin{pmatrix} x \\ y \\ z \end{pmatrix} = \begin{pmatrix} a_e \cos(\vartheta)\cos(\varphi) + x_e \\ b_e \cos(\vartheta)\sin(\varphi) + y_e \\ c_e \sin(\vartheta) + z_e \end{pmatrix}. \quad (2)$$

The dimensional parameters read (in au) $a_e = 100$, $b_e = 100$, $c_e = 120$, $x_e = -15$, $y_e = 0$, and $z_e = 0$, which implies heliocentric distances toward the poles of 120 and 85 au (upwind) and 115 au (downwind) in the x-z plane.

Throughout this paper, we use spherical coordinates with longitude φ, latitude ϑ, and heliocentric distance R. The reference frame is a rotated ecliptic coordinate system centered in the Sun: The x-axis points from the Sun to the nose or upstream direction ($\varphi = 0°$, $\vartheta = 0°$), corresponding to $\lambda \approx 256°$, $\beta \approx 5°$ in ecliptic longitude and latitude (McComas et al. 2015). The z-axis lies inside the plane spanned by the x-axis and the north pole of the ecliptic (i.e., 5° offset from the ecliptic North pole), and the y-axis closes the right-handed system. An illustration of this coordinate system and the heliospheric shapes in the x-z plane are shown in Figure 2.

The global shape of the heliosphere outside the nose region is unknown; for an overview of the possible solutions see, e.g., Pogorelov et al. (2017) and Opher (2016) and also consider Dialynas et al. (2017) and Schwadron & Bzowski (2018). We therefore experiment with three different heliopause shapes: they all conform with the upwind standoff distance known from the *Voyager* crossings at 122 and 119 au (Stone et al. 2013). Two of the heliopause shapes are ellipsoids with an offset relative to the Sun in analogy to the termination shock (also see Fahr et al. 1986). The dimensional parameters in Equation (2) for our case of a "small ellipsoid" heliopause read in units of au: $a_e = 255$, $b_e = 358$, $c_e = 363$, $x_e = -140$, $y_e = 0$, and $z_e = 35$. These parameters become $a_e = 510$, $b_e = 474$, $c_e = 480$, $x_e = -395$, $y_e = 0$, and $z_e = 35$ for the case of a "large ellipsoid" with an extended heliosheath region in the downwind direction. In addition to these ellipsoids, we also implemented the cylindrical Parker shape for the heliopause (Parker 1961; Röken et al. 2015):

$$\begin{pmatrix} x \\ y \\ z \end{pmatrix} = \begin{pmatrix} (2a_e^2 - \rho^2)\big/(\sqrt{4a_e^2 - \rho^2}) \\ \rho\cos(\varphi) \\ \rho\sin(\varphi) \end{pmatrix}, \quad (3)$$

with the standoff distance $a_e = 115$ au at the x-axis and the cylindrical coordinates φ and ρ (radial distance from x-axis). The cylindrical shape and the ellipsoids are symmetric with respect to the x-axis. They can thus be characterized by their cross sections in the x-z plane as illustrated in Figure 2. Additional geometric shapes for the termination shock or the heliopause could easily be implemented, but we will restrict the discussion in Section 3 to these three cases as they cover a wide range of possible geometries. The inner heliosheath thickness of 150–220 au toward the poles for the ellipsoids is motivated by Galli et al. (2016) and Reisenfeld et al. (2016). A reanalysis of the method from Reisenfeld et al. (2016) showed that the temporal variations of ENA intensities imply a much shorter heliosheath thickness of only 50 au toward the poles (Reisenfeld et al. 2019). This value is consistent with the cylindrical shape (see Figure 2).

2.2. Neutral Densities

Inside the heliopause, we assume a constant neutral hydrogen density $n_{\rm H} = 0.1\,{\rm cm}^{-3}$. This is correct within a factor of 2 (Schwadron et al. 2011; Heerikhuisen et al. 2014; Gloeckler & Fisk 2015), and because we scale the ion intensities in such a way as to reproduce the observed ENA intensities, the explicit value is irrelevant in our code. The same holds true for ENA sources in the outer heliosheath. Here, $n_{\rm H}$ would be $0.2\,{\rm cm}^{-3}$ within a factor of 2 for all regions including the hydrogen wall (Müller & Zank 2004; Gloeckler & Fisk 2011; Heerikhuisen et al. 2014; Opher et al. 2016).

2.3. Charge-exchange Cross Sections

The charge-exchange cross section $\sigma(E)$ depends on energy but is well known (Barnett 1990; Lindsay & Stebbings 2005). We rely on the semi-empirical formula by Lindsay & Stebbings (2005) to calculate $\sigma(E)$ for the reaction $H^+ + H \rightarrow H^* + H^+$.

2.4. ENA Loss Processes

ENA loss processes are so far included in a crude manner: inside the heliopause, ENA losses are neglected. More precisely, the actual ENA losses amount to less than 10% for the proton densities in the inner heliosheath of $n_p = 10^{-3} \ldots 10^{-2}\,{\rm cm}^{-3}$ expected from models (Opher et al. 2016; Pogorelov et al. 2017). The proton distribution of our empirical model implies $n_p = 0.01\,{\rm cm}^{-3}$ with a radial plasma bulk speed $u_R = 100\,{\rm km\,s}^{-1}$ in the heliosheath (see Section 2.5.2).

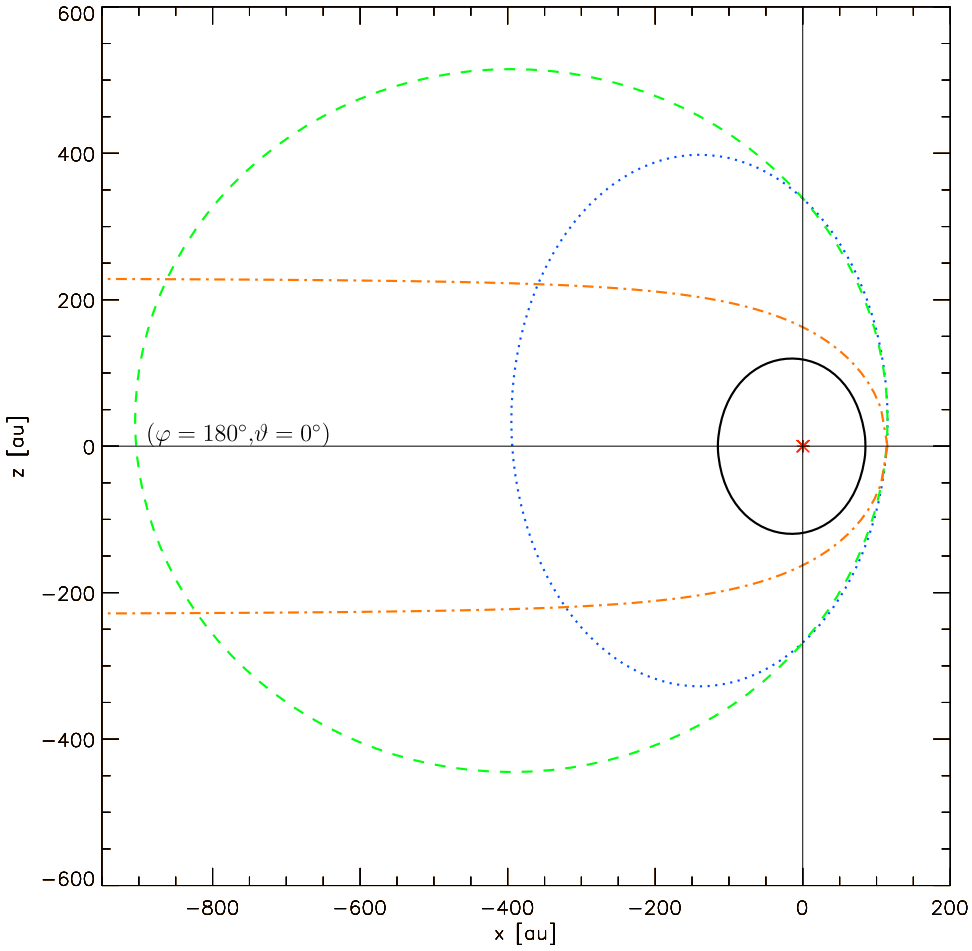

Figure 2. Shapes of the termination shock (black solid line) and the three different heliopause cases (blue dotted line: small ellipsoid; green dashed line: large ellipsoid; orange dashed–dotted line: cylindrical Parker model) assumed in this study. The Sun (red asterisk) is situated at the center of the coordinate system; the x-axis from the Sun to the nose of the heliosphere points to $\varphi = 0°$, $\vartheta = 0°$ in polar coordinates.

Outside the heliopause, a constant $n_p = 0.1\ \mathrm{cm}^{-3}$ is assumed; heliospheric models typically predict a range of 0.05 ... 0.1 cm^{-3} for the region of a few hundred au beyond the heliopause (Opher et al. 2016; Pogorelov et al. 2017). Therefore, the following ENA loss $L(E)$ is subtracted from the ENA source term in Equation (1):

$$L(E) = \int_{\mathrm{LOS}} dl\, j_{\mathrm{ENA}}(E) n_p\, \sigma(E). \tag{4}$$

Equation (4) implies a mean free path length of 392 au for a 1 keV ENA beyond the heliopause, i.e., after that path length, the original ENA intensity has decreased to $1/e$.

2.5. Proton Distributions

By far the most difficult and important task for any heliospheric ENA model is to generate the full intensity distribution $j_p(E)$ of all proton populations at any given place. Calculating the local proton density is a first step but not sufficient to predict maps of ENA intensities, because the full angular and energy distribution of $j_p(E)$ would be required. This is the main reason why we resorted to the simple empirical approach to predict ENA maps at this stage of investigation. More specifically, we defined for each of the three regions (inside termination shock, inner heliosheath between termination shock and heliopause, and beyond heliopause) the parent proton populations $j_p(E)$ giving rise to observable ENAs in the energy range of interest.

2.5.1. Supersonic Solar Wind inside the Termination Shock

Inside the termination shock, we only consider neutralized protons originating from the supersonic solar wind; pickup ions reneutralized inside the termination shock are neglected so far. For the solar wind parameters we assume a constant $v_p = 440\ \mathrm{km\ s}^{-1}$ ($E_p = 1.0$ keV) representative for low heliolatitudes (Khabarova et al. 2018) and $n_p(r) = 8\ \mathrm{cm}^{-3} \times (1\ \mathrm{au}/r)^2$ (Gosling et al. 2007). The energy distribution of the solar wind around the mean energy at a specific moment in time depends on heliocentric distance, heliolatitude, and solar activity. We approximate this energy distribution $J(E)$ with a rectangular function centered on $440 \pm 80\ \mathrm{km\ s}^{-1}$, based on long-term averages of *Voyager 2* and *New Horizons* solar wind data between 11 and 31 au close to the ecliptic plane (Gosling et al. 2007; Elliott et al. 2016):

$$J(E) = \begin{pmatrix} \frac{F_0}{0.7\ \mathrm{keV}}, & \text{if } 0.7\ \mathrm{keV} \leqslant E \leqslant 1.4\ \mathrm{keV} \\ 0, & \text{else} \end{pmatrix}. \tag{5}$$

The angular distribution of the solar wind intensity is defined by the FWHM angle around the bulk direction of $\alpha_0 = 5°$, which corresponds to a typical solar wind temperature of

1.2×10^5 K (Marsch et al. 1982; Gosling et al. 2007; Galli et al. 2013).

2.5.2. Shocked Solar Wind and Shocked Pickup Ions in the Inner Heliosheath

Assuming that the globally distributed heliospheric ENA flux apart from the *IBEX* ribbon (McComas et al. 2014) and the INCA belt (Krimigis et al. 2009) derives from the inner heliosheath (Galli et al. 2016), and disregarding any temporal or spatial variations of that signal, we can use the ENA measurements made with *IBEX* (Funsten et al. 2009; Fuselier et al. 2009), INCA, and other ENA cameras as input for $j_p(E)$. If $j_{\rm HS}$ is the intensity of the globally distributed ENA signal at 100 au in the inertial reference frame, the proton intensity giving rise to these measured ENAs simply is

$$j_p(E) = \frac{j_{\rm HS}(E)}{(d_{\rm HP} - d_{\rm TS}) n_{\rm H}\, \sigma(E)}, \quad (6)$$

provided that the proton intensities inside the heliosheath are isotropic and constant along a radial LOS from termination shock to heliopause. Parameters $d_{\rm TS}$ and $d_{\rm HP}$ denote the radial distances to the termination shock and the heliopause, respectively. The $j_{\rm HS}(E)$ in Equation (6) is approximated as a continuous sequence of power laws based on ENA observations as

$$j_{\rm HS}(E) = j_0 (E/E_0)^{\gamma}. \quad (7)$$

For $E = 10$–50 eV, the power-law exponent γ is 0.72 if the heliosheath proton distribution rolls over (Galli et al. 2016, 2017), or $\gamma = -0.43$ if the energy spectrum gets flatter but does not roll over (Zirnstein et al. 2018). For 50 eV–1 keV, $\gamma = -1.1$, steepening to $\gamma = -2.0$ from 1 to 16.4 keV (based on *IBEX*-Lo and *IBEX*-Hi observations from 2009 to 2012 at energies 50 eV–6 keV; Galli et al. 2016), and then dropping rapidly with $\gamma = -4.0$ from 16.4 to 100 keV based on high-energy ENA measurements with INCA (Krimigis et al. 2009), HENA (Kallenbach et al. 2005), and HSTOF (Hilchenbach et al. 1998). This ENA energy spectrum and its observational basis are illustrated in the top panel of Figure 3. For this spectrum, only ENA measurements from the upwind heliosphere direction were used whenever available. However, for energies below 500 eV we had to rely on downwind hemisphere measurements because of the very intense ISN signal appearing in the upwind hemisphere in *IBEX*-Lo data (Galli et al. 2014). The single spectrum in Figure 3 implies that the heliospheric ENAs at solar wind energies and below can be described by a spatially uniform, globally distributed flux (GDF) except for the ENA ribbon (Schwadron et al. 2014; Galli et al. 2016).

The proton intensities in the inner heliosheath are modified by default by plasma loss processes. Based on the concept of a plasma cooling length l_c (Schwadron et al. 2011; Galli et al. 2017) and a constant radial plasma bulk flow of $u_R = 100\,{\rm km\,s^{-1}}$,

$$l_c(E) = \frac{u_R}{v_{\rm ENA}(E) n_{\rm H}\, \sigma(E)}, \quad (8)$$

we expect $l_c = 350$, 166, and 57 au for 10 eV, 100 eV, and 10 keV, respectively. The cooling length over the full energy range from 10 eV to 100 keV is plotted in the bottom panel of Figure 3. The plasma bulk flow speed u_R is, in principle, not constant throughout the heliosheath (Zirnstein et al. 2016b). However, these authors show that the variability between different models is as large as the modeled spatial variations. We therefore chose one global constant of $u_R = 100\,{\rm km\,s^{-1}}$ between the *Voyager 1* ($40\,{\rm km\,s^{-1}}$) and *Voyager 2* ($140\,{\rm km\,s^{-1}}$) speed measurements (Schwadron et al. 2011; Gloeckler & Fisk 2015). For any u_R, protons around 10 keV energies happen to have the shortest cooling length, whereas l_c increases again to several hundred au for higher ENA energies. This implies that ENA energies below 500 eV or above 50 keV are more appropriate than intermediate energies to image large heliosheath dimensions (DeMajistre et al. 2018). Hydrogen ENAs at keV or tens of keV energy are indicative of the plasma distribution just beyond the termination shock.

We implemented plasma cooling in our empirical model via Equation (8) and by assuming an exponential decrease of the local ion j_p over the distance x (radial distance from local plasma region to closest point at termination shock). This results in a modified proton intensity of

$$\tilde{j}_p = j_p \frac{l_{\rm HS}}{l_c} \frac{\exp(-x/l_c)}{(1 - \exp(-l_{\rm HS}/l_c))}. \quad (9)$$

The inner heliosheath thickness $l_{\rm HS}$ denotes the radial distance between the termination shock and the heliopause. The dimensionless normalization factor ensures that the modified proton intensity, inserted into the basic ENA equation (Equation (1)), reproduces the observed input ENA intensity at 1 au. If the heliosheath thickness exceeds $10 l_c$ for a specific heliosphere model (see Section 2.1), it is set to $10 l_c$.

Equation (9) is based on a simplification, as we assume radially symmetric plasma streamlines in the heliosheath. In reality, they would be curved to some extent in the flanks and toward the poles of the heliosphere, but the predicted curvatures also depend on the specific model (see, e.g., Izmodenov & Alexashov 2015; Pogorelov et al. 2017). Our empirical model does not contain plasma streamlines for the different heliosphere shapes, and the effect would not drastically change the predicted ENA maps anyway. Let us consider the case of largest deviations, i.e., a viewing direction toward $+z$ for the case of the large ellipsoid heliopause and ENA energies corresponding to $l_c = l_{\rm HS}$ (Equation (8)): with Equation (9) and radial streamlines, half of the total ENA intensity from the heliosheath along the polar LOS (Equation (1)) is contributed by plasma between the termination shock and $0.38 l_{\rm HS}$ within the heliosheath. Curved plasma streamlines (Izmodenov & Alexashov 2015; Pogorelov et al. 2017) would narrow these ENA emissions slightly, i.e., the ENA half-length would reduce to a value of $(0.30...0.38) l_{\rm HS}$. For viewing directions toward the nose and the downwind hemisphere, deviations of streamlines from radial symmetry are even smaller, and for cooling lengths much shorter or longer than the heliosheath thickness, the effect of curved streamlines on ENA maps would also become weaker.

2.5.3. Heliospheric ENA Sources beyond the Heliopause: The IBEX Ribbon

We assume that the *IBEX* ribbon of increased ENA intensities around solar wind energies is caused by so-called secondary ENAs (see, e.g., McComas et al. 2014, 2017;

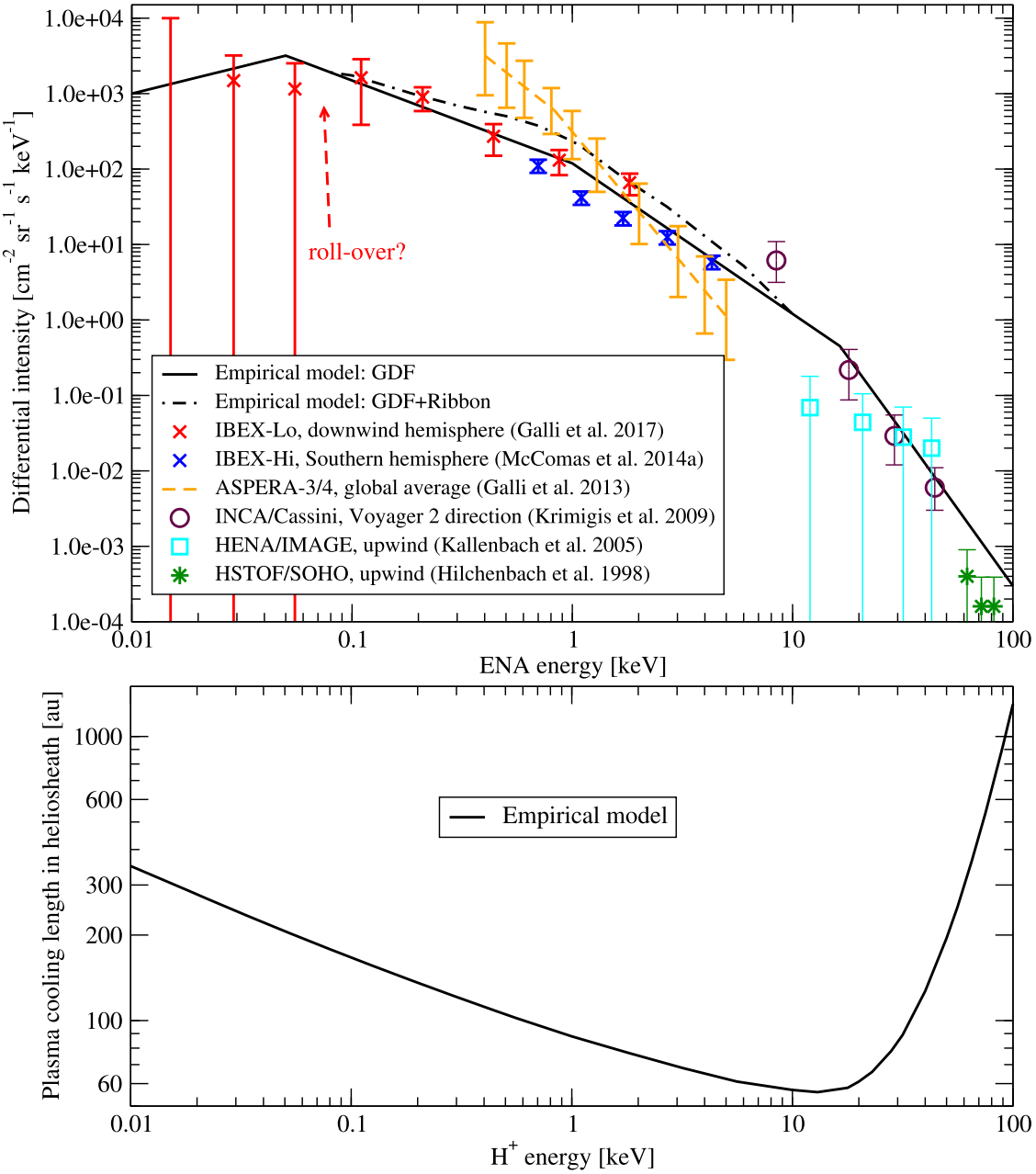

Figure 3. Energy spectra of heliospheric ENAs (top panel). The spectra assumed for the empirical model are plotted as black solid (globally distributed flux) and dashed–dotted lines (GDF plus *IBEX* ribbon ENAs); previous observations are added as symbols. The bottom panel shows the plasma cooling length in the heliosheath as a function of the proton energy corresponding to the ENA energy in the top panel.

Swaczyna et al. 2016; Zirnstein et al. 2016a; Fuselier et al. 2018; Dayeh et al. 2019; but see also Sylla & Fichtner 2015 for an alternative explanation). The secondary ENA hypothesis explains the ribbon as being due to neutralized solar wind and picking up protons that cross the termination shock and the heliopause, and are then reionized and start gyrating around the interstellar magnetic field just beyond the heliopause before charge-exchanging again with the ISN hydrogen. Again, we rely on

$$j_p(E) = \frac{j_{\mathrm{Ribbon}}(E)}{d_{\mathrm{Ribbon}}\, n_{\mathrm{H}}\, \sigma(E)}, \tag{10}$$

with $j_{\mathrm{Ribbon}}(E) = 250,\ 250,\ 200,\ 100,\ 35,\ 15,\ 4.5,$ and $0\,\mathrm{cm^{-2}\,sr^{-1}\,s^{-1}\,keV^{-1}}$ for energies 0.1, 0.5, 0.7, 1.1, 1.7, 2.7, 4.3, and 6 keV, respectively, based on *IBEX* measurements (Galli et al. 2016; McComas et al. 2017). This energy spectrum is shown as the dashed–dotted line in Figure 3.

As for the globally distributed ENA flux, temporal and spatial variations along the ribbon are not implemented yet. In particular, the latitudinal dependence of maximum ENA intensity with ENA energy (McComas et al. 2017; Desai et al. 2019) is not included yet. Contrary to the globally distributed ENA flux from the inner heliosheath, these ENA contributions are narrowly constrained in angular width and probably in thickness of their source of origin: For a region outside the heliopause to produce ribbon ENAs along the LOS of an observer, two conditions must be met: First, the LOS vector $\boldsymbol{r}$ must be nearly perpendicular to the local direction of the interstellar magnetic field $\boldsymbol{B}$ (McComas et al. 2014;

Swaczyna et al. 2016), i.e., $\hat{\boldsymbol{B}} * \hat{\boldsymbol{r}} \approx 0$ for the normalized vectors $\hat{\boldsymbol{B}}$ and $\hat{\boldsymbol{r}}$. The emitted ENA intensity drops off for an observer LOS offset with respect to the $\hat{\boldsymbol{B}} * \hat{\boldsymbol{r}} = 0$ surface as $j_p \exp(-\alpha^2/(2\alpha_0^2))$; the offset angle is defined as $\alpha = |\arccos(\hat{\boldsymbol{B}} * \hat{\boldsymbol{r}}) - 90°|$, and the scaling factor $\alpha_0 = 5°$ is derived from the thermal spread of the solar wind (see Section 3.1.3). The ribbon ENA intensity is set to zero whenever α exceeds a user-defined half width of 10°. Second, the location must be adjacent to the heliopause at a heliocentric distance shorter than or equal to the sum of the heliopause heliocentric distance plus the ribbon thickness. For the latter we assumed a global radial thickness of $d_{\mathrm{Ribbon}} = 40$ au (Swaczyna et al. 2016). The actual heliocentric distance of the ribbon region thus depends on the heliosphere shape and viewing direction.

To directly compare our predictions and recommended spacecraft trajectories to *IBEX* measurements we parameterized the ENA ribbon as a ring-shaped emission around a symmetry axis, i.e., the ribbon center $\hat{\boldsymbol{r}}_{\mathrm{Rb}}$. The local direction of the interstellar magnetic field for a given point at the heliopause thus is

$$\hat{\boldsymbol{B}} = \mathfrak{R}_{15} \begin{pmatrix} \cos(\vartheta_{\mathrm{Rb}})\cos(\varphi_{\mathrm{Rb}}) \\ \cos(\vartheta_{\mathrm{Rb}})\sin(\varphi_{\mathrm{Rb}}) \\ \sin(\vartheta_{\mathrm{Rb}}) \end{pmatrix}. \tag{11}$$

The ribbon center $\hat{\boldsymbol{r}}_{\mathrm{Rb}}$ is defined by $\varphi_{\mathrm{Rb}} = -36°$, $\vartheta_{\mathrm{Rb}} = +35°$ in our coordinate system, in accordance with the observed ribbon center $(\lambda, \beta) = (220.^\circ3, 40.^\circ5)$ (Dayeh et al. 2019) or $(219.^\circ2, 39.^\circ9)$ (McComas et al. 2017) in ecliptic coordinates and the upwind direction of $(\lambda = 255.^\circ7, \beta = 5.^\circ1)$ (McComas et al. 2015). The rotation matrix $\mathfrak{R}_{15}$ rotates $\hat{\boldsymbol{B}}$ by 15° away from the viewing direction in the $(\hat{\boldsymbol{r}}, \hat{\boldsymbol{r}}_{\mathrm{Rb}})$-plane. As a result, the opening angle of the ENA ribbon emission equals the observed radius of 75° (Dayeh et al. 2019) instead of 90°.

Other potential ENA sources from the outer heliosheath are neglected in this study. For instance, the flow of interstellar plasma along the heliopause is expected to produce a narrow fan of low-energetic ENAs around the nose of the heliosphere. Judging from the analogy to the subsolar ENA jets observed at Mars with *Mars Express* (Futaana et al. 2006), we expect an integral ENA intensity on the order of $10^6\,\mathrm{cm^{-2}\,sr^{-1}\,s^{-1}}$ between the heliopause and the bow shock or bow wave. However, the energy of these ENAs would be concentrated around 3 eV (corresponding to the ISN flow speed of $25\,\mathrm{km\,s^{-1}}$) and thus cannot be readily detected with conventional ENA instruments (Wurz 2000).

2.6. Proper Motion of Spacecraft

Finally, the derived integral ENA intensity at the observer may be modified by the proper motion of the observer. For the *Interstellar Probe*, a radial velocity of 10–20 au $\mathrm{yr^{-1}}$ is foreseen (McNutt et al. 2018; Brandt et al. 2019), which translates to a spacecraft velocity of $u_{\mathrm{sc}} \approx 50 \ldots 100\,\mathrm{km\,s^{-1}}$. This is not much lower than the speed of a 100 eV hydrogen ENA in the heliosphere rest frame ($v_{\mathrm{ENA}} = 138\,\mathrm{km\,s^{-1}}$). The resulting Compton–Getting effect increases low-energy ENA intensities from ram direction and decreases those observed from anti-ram direction. In our model, we assume for simplicity's sake that the spacecraft is moving radially away from the Sun with a user-defined speed of the spacecraft relative to the heliosphere between $u_{\mathrm{sc}} = 0$ and $100\,\mathrm{km\,s^{-1}}$. The intensity of an ENA signal following a power law (Equation (7)), observed at an angle φ relative to the spacecraft velocity vector, is then modified by (Ipavich 1974; Roelof et al. 1976; McComas et al. 2010)

$$\tilde{j}_{\mathrm{ENA}} = j_{\mathrm{ENA}} \left(1 - 2\cos(\varphi)\frac{u_{\mathrm{sc}}}{v_{\mathrm{ENA}}} + \frac{u_{\mathrm{sc}}^2}{v_{\mathrm{ENA}}^2}\right)^{(\gamma-1)}. \tag{12}$$

3. Model Implications for Future Heliospheric Missions

The main scientific question to be answered with heliospheric ENA imaging can be formulated as follows: How does the heliosphere interact with its galactic neighborhood, and what is the three-dimensional structure of the heliospheric interface? The results of our empirical ENA model give some guidelines for an ENA imager at large heliocentric distance. In the following, we will mostly discuss the technical requirements of an ENA instrument and assess the spacecraft trajectory most beneficial for heliospheric ENA imaging. For the latter, we will focus on the geometrical aspects, i.e., parallax effects and the opportunity to directly image plasma boundaries at large heliocentric distances. Parallax observations have already been used in the context of *IBEX* observations: Swaczyna et al. (2016) used parallax observations to constrain the distance of the *IBEX* ribbon to Earth. For a parallax baseline of $2R$ and a parallax angle 2μ, the distance to the object calculates to

$$d = \frac{R}{\tan(\mu)}. \tag{13}$$

Obviously, the longer the baseline $2R$, the easier the parallax angle can be observed in ENA maps. For the *IBEX* baseline of 2×1 au, the observed $\mu = 0.^\circ41$ implied $d = 140^{+84}_{-38}$ au (Swaczyna et al. 2016). Having a longer baseline would drastically reduce this uncertainty and would thus rule out some theories about the nature of the *IBEX* ribbon.

In addition to the geometrical aspects, observing heliospheric ENAs at large heliocentric distances also offers benefits in terms of lower background sources (see Section 3.1.2) and higher ENA survival probabilities. However, lower background rates can be achieved just by moving the spacecraft from Earth orbit to the Lagrange 1 point of the Sun–Earth system, which is the approach for the upcoming *IMAP* mission (McComas et al. 2018). The second benefit derives from the survival probabilities of heliospheric ENAs increasing with distance to the Sun: ENAs traveling to the inner solar system may be reionized, and their trajectories are affected by solar radiation pressure and solar gravity (Bzowski 2008; Bzowski et al. 2013). However, these effects are most relevant for low-energy ENAs with tens of eV. For ENAs of 100 eV or more, the survival probability to reach 1 au is at least 0.35 for any place of origin in the heliosheath (Galli et al. 2016).

3.1. Recommendations for ENA Instrument Specifications

3.1.1. Energy Range

Each part of the heliospheric ENA energy range provides important information about the heliosphere and its plasma populations. On the other hand, every ENA energy range has its own observational challenges (Wurz 2000). The general appearance of the heliosphere as seen in ENAs changes dramatically for different energies. Figure 4 illustrates this for 0.1, 1, and 10 keV ENAs as seen from a vantage point in the

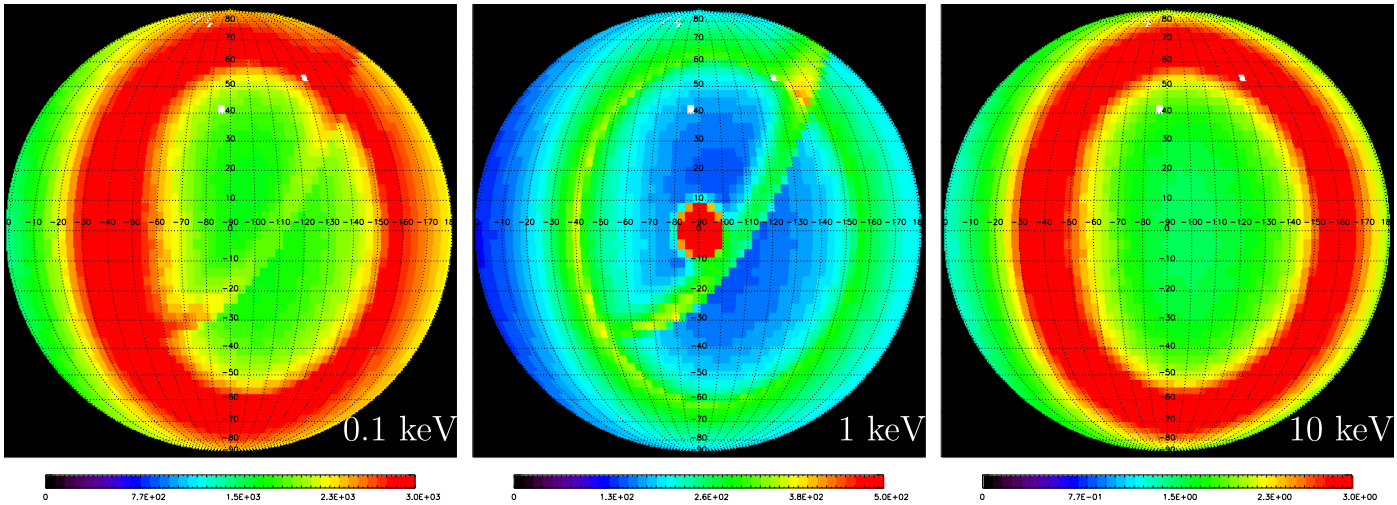

Figure 4. ENA map predictions for an observer inside the heliosheath at 120 au heliocentric distance for the case of a small ellipsoid heliosphere. From left to right: ENA energies of 0.1, 1, and 10 keV (note the different intensity color scale). The observer is located inside the ecliptic plane in the flank of the heliosheath ($\varphi = 90°$, $\vartheta = 0°$), looking back to the Sun in the map center.

inner heliosheath at 120 au heliocentric distance in the flank region ($\varphi = 90°$, $\vartheta = 0°$) of a small ellipsoid heliosphere.

The protons giving rise to low-energy ENAs (roughly 50–500 eV) dominate, by their sheer number, the plasma pressure in the inner heliosheath toward the flanks and downwind hemisphere (Galli et al. 2017). The pressure derived for the GDF (i.e., the heliospheric ENA signal minus the *IBEX* ribbon) is dominated by the energies from 30 to 500 eV for any heliospheric direction (Livadiotis et al. 2013). The physics of the heliosheath therefore can only be understood by observing ENAs in this energy range. One of the outstanding questions in this regard is whether the energy spectrum of the GDF rolls over around 100 eV (see Figure 3). The answer to this question would help determine the importance of pickup ions in the heliosheath and whether the GDF indeed is produced solely by plasma sources from the inner heliosheath (Galli et al. 2017; Zirnstein et al. 2018). Detecting low-energy ENAs at a reasonable signal-to-noise ratio is technically more challenging than for energies $\gg$1 keV. Below 300 eV, only the surface conversion technique (Wurz 2000) gives reasonable ENA detection efficiencies. That technique was successfully used by NPD/ASPERA-3&4 (Barabash et al. 2006, 2007) and *IBEX*-Lo (Fuselier et al. 2009) to detect heliospheric ENAs. *IBEX*-Lo results revealed the energy spectrum of heliospheric ENAs down to roughly 100 eV, but for lower energy the uncertainties, introduced by low count statistics and strong background sources (Wurz et al. 2009), made the interpretation of the results difficult (Fuselier et al. 2014; Galli et al. 2014). Some of the local background sources encountered by *IBEX*-Lo could be avoided by an interplanetary or interstellar ENA imager (e.g., background from Earth's magnetosphere; Galli et al. 2016), whereas other sources, in particular ISN atoms, might persist at other places inside the heliosphere. For a spacecraft moving away from the Sun at 20 au yr^{-1} or faster, low-energy ENAs ($\leqslant$50 eV) from the anti-ram direction would not reach the spacecraft anymore, whereas the low-energy ENAs from the ram hemisphere would be easily detectable.

Solar wind energies (from 500 eV to several keV) are obviously vital to study the *IBEX* ribbon in more detail at various heliocentric distances. For these ENA energies, several detection techniques (such as conversion surfaces or conversion foils to ionize the ENAs) are available (Wurz 2000), and the corresponding speed of these ENAs usually is well above the proper motion of any spacecraft. On the other hand, protons of solar wind energy have the shortest mean free path length in the heliosheath because of plasma cooling (see Equation (8)). Thus, they are not useful to reveal the large structures of the heliosphere outside the nose region.

High-energy ENAs above 50 keV, in contrast, have mean free path lengths of hundreds of au in the heliosheath (DeMajistre et al. 2018). These ENAs represent suprathermal plasma ions and energetic particles in the heliosheath rather than the bulk plasma. The question remains whether ENA intensities (and their variation with time) at these energies reveal the actual dimension of the heliosphere (Dialynas et al. 2017; Schwadron & Bzowski 2018). In any case, observing these high-energy ENAs is indispensable to understand acceleration processes at the plasma boundaries of the heliosphere (McComas et al. 2018).

Since the detection techniques and instruments required to measure low-energy and high-energy ENAs differ strongly, at least two different ENA imagers should be foreseen to cover the full range relevant for heliospheric ENAs. One option is to rely on three ENA imagers whereby the low ENA imager serves a double function to also detect ISN (for ram observations close to Earth orbit, ISN energies range from roughly 10 to 600 eV for most common ISN species). This approach is adopted by the upcoming *IMAP* mission with *IMAP*-Lo (10 eV–1 keV), *IMAP*-Hi (0.4–16 keV), and *IMAP*-Ultra (3–300 keV) (McComas et al. 2018). Another option could be to use a mass spectrometer for the ISN species and to cover the heliospheric ENA energy spectrum with just two ENA instruments (covering the ranges from 20 eV to a few keV and from a few keV to several tens of keV). This approach has the drawback that redundancy and energy overlap from 1 to 10 keV between the two ENA instruments might be lacking. Having overlapping energies allows for cross-calibration between different ENA instruments in space (Reisenfeld et al. 2016; McComas et al. 2017). This is very helpful, as absolute calibration of ENA instruments is notoriously difficult (Fuselier et al. 2009, 2012).

Since the whole energy range is relevant, we will use the three ENA energies of 0.1, 1, and 10 keV as points of reference in the subsequent discussion of spacecraft trajectories for an ENA imager at great heliocentric distance (Section 3.2).

3.1.2. ENA Detection Limits, Signal-to-noise Ratio, and Relative Uncertainty

The recommended ENA detection limits obviously depend on the ENA energy range of the instrument as illustrated in Figure 3. The signal-to-noise ratio of *IBEX*-Lo data, e.g., turned out to be 1–10 for energies above 100 eV, depending on viewing direction (Galli et al. 2017; McComas et al. 2017). The expected signal-to-noise ratio of *IMAP*-Lo and *IMAP*-Hi is higher than 50 (McComas et al. 2018) for ENA energies of several hundred eV. However, the limiting factor for ENA images measured with *IBEX*-Lo turned out to be not the signal-to-noise ratio or low count statistics but rather strong background sources that could not be reduced by longer integration times (Galli et al. 2014, 2016). These background sources can be caused by penetrating radiation, by UV light, or by ions created within the instrument that are then post-accelerated (Wurz 2000; Fuselier & Pope 2005; Funsten et al. 2009; Wurz et al. 2009).

Background and noise levels are very specific to a given mission and instrument design. General signal-to-noise or signal-to-background ratios for an interstellar ENA imager therefore would have to invoke too many assumptions to serve as useful recommendations. For the present study we rather ask the following question: What is the minimum significant change in ENA intensity if we assume an instrument measuring the ENA intensity from a given heliosphere region at an angular resolution of a few degrees (i.e., the instrument field of view) from two different observer positions?

A look at 10 yr of *IBEX* measurements and data analysis is enlightening here: for *IBEX*-Lo, the limit for a significant intensity change is 30% for solar wind energies and increases to at least 50% for energies below 100 eV (Fuselier et al. 2012; Galli et al. 2016). *IBEX*-Hi has better signal-to-noise and signal-to-background ratios than *IBEX*-Lo for energies above 1 keV; the relative uncertainty for a field-of-view-sized map pixel ($6^\circ \times 6^\circ$) ranges between 10% and 20% (Fuselier et al. 2014; Reisenfeld et al. 2016; Galli et al. 2017; McComas et al. 2017). If *IBEX*-Hi data are integrated over a larger region in the sky (see the Appendix in McComas et al. 2019) or over several months, the relative uncertainty can be reduced to a few percent for ENA energies above 1 keV (Reisenfeld et al. 2016; McComas et al. 2017). Based on these experiences, we will assume for the subsequent section a critical difference of 10% for all ENA energies. This is to be the minimum relative change in ENA intensity over a single map pixel identifiable by an ENA instrument on a spacecraft at large heliocentric distance.

3.1.3. Angular Resolution

The finest spatial structures in our ENA model are currently the plasma boundaries. Other spatial structures necessitating higher spatial resolution may exist, but they are not implemented yet in our current model. Fine structures in the *IBEX* ribbon with an angular separation of a few degrees were predicted, e.g., by Giacalone & Jokipii (2015) and McComas et al. (2018), and such turbulence-induced fine structures would change the observed ribbon ENA intensities at a 2° scale within a year (Zirnstein et al. 2019). The only angular resolution inherent to our current model is the thermal spread of the solar wind, $\alpha_0 = 5^\circ$. Upcoming and proposed ENA imaging missions indeed aim at a similar or better spatial resolution: for *IMAP*, 9°, 4°, and 2° are foreseen depending on ENA energy (McComas et al. 2018); for a LIMO type of ENA imager at a few au heliocentric distance, an angular resolution of 1° is proposed (Barabash et al. 2019).

If we assume, for instance, an angular resolution of 1° and an ENA intensity of $100\,\mathrm{cm^{-2}\,sr^{-1}\,s^{-1}\,keV^{-1}}$ at 1 keV energy (see Figure 3), we expect triple coincidence count rates of 10^{-4} to $10^{-3}\,\mathrm{s^{-1}}$ for detection efficiencies similar to *IBEX*-Lo (Fuselier et al. 2009) and *IBEX*-Hi (Funsten et al. 2009) and a geometric factor reduced by 36 compared to the $6^\circ \times 6^\circ$ angular resolution for *IBEX*. This implies that a few weeks would be enough to accumulate hundreds of ENA counts and thus to obtain a statistically solid result at 1° resolution at solar wind energies. The limiting factor for angular resolution might again be the instrument-related background rates. In the following discussions, we will use 3° as the default angular resolution.

3.2. Which Spacecraft Trajectories Are Most Interesting for Heliospheric ENA Imaging?

Assuming that we have one or several ENA instruments on board a spacecraft heading to heliocentric distances beyond Earth, which trajectory is most rewarding? An actual mission concept for an interstellar probe obviously will have to balance the science cases from many different fields, such as heliosphere physics, planetary sciences, and astronomy (Brandt et al. 2019). Here, we restrict ourselves to the question of which vantage points are useful to better understand the GDF and the ribbon ENAs and to determine the shape of the heliosphere. To this end, we created hemispherical ENA maps at 0.1, 1, and 10 keV from an assumed observer position anywhere inside or outside the heliosphere for any of the three heliosphere shapes. We structure the discussion of the model results the following way:

1. Spacecraft on a circular orbit close to the ecliptic plane at a heliocentric distance between 2 and 10 au (Section 3.2.1).
2. Spacecraft on a radial escape trajectory. For symmetry reasons, we only consider the quadrant covering the northern hemisphere from the upwind to downwind direction on the port side of the heliosphere (Section 3.2.2):
   (2a) Close to the ecliptic plane and headed toward the nose ($\varphi = 0^\circ$, $\vartheta = 0^\circ$).
   (2b) $\varphi = 45^\circ$, $\vartheta = 0^\circ$.
   (2c) $\varphi = 90^\circ$, $\vartheta = 0^\circ$ (toward heliosphere flank).
   (2d) $\varphi = 90^\circ$, $\vartheta = +30^\circ$ (above the ecliptic plane).
   (2e) $\varphi = 180^\circ$, $\vartheta = 0^\circ$ (downwind direction, close to ecliptic plane).

We will neglect Compton–Getting effects on ENA intensities for all trajectories to eliminate an additional free parameter and to improve comparability between the different scenarios. Neglecting the proper motion of the spacecraft relative to the heliospheric ENAs is justified for a circular trajectory at large heliocentric distance. For a radial escape trajectory, the ENA intensities seen from the Sun direction would decrease, and those seen from the anti-Sun hemisphere would increase. The observed intensity would change to 0.3 and 6.7 times the inertial intensity for the lowest considered

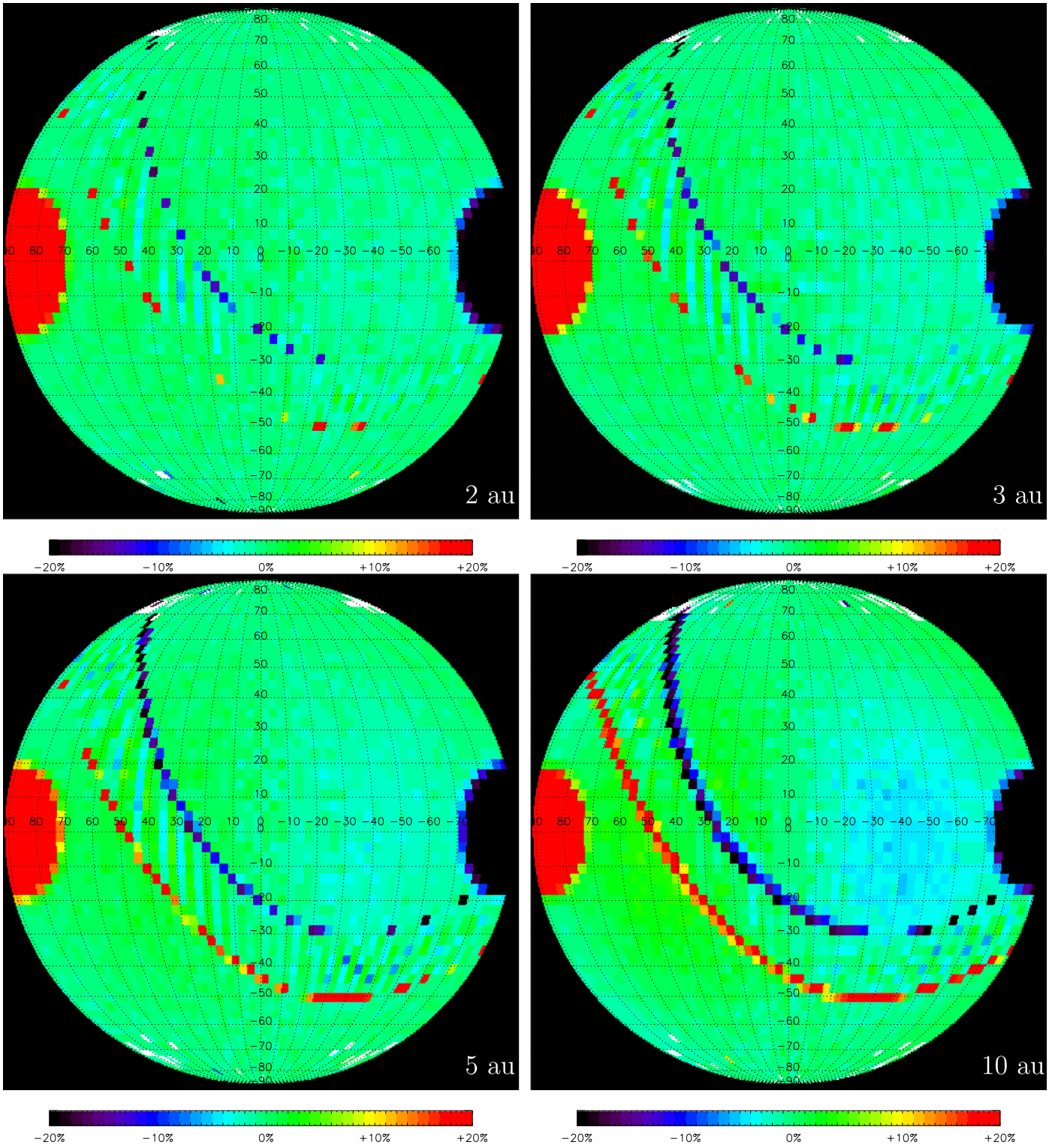

Figure 5. Relative differences of predicted ENA intensities for the upwind hemisphere when observed from the opposite positions at $\varphi = 90°$ and $\varphi = 270°$ from a circular orbit at 2 au (top left) to 10 au (bottom right). ENA energy = 1 keV, angular resolution = 3° × 3°, large ellipsoid assumed as heliosphere shape. Relative differences are detectable if pixels are blue or yellow (at least ±10% relative difference). The ribbon parallax feature becomes clearly visible across the hemisphere from heliocentric distances greater than 2 au; the semicircles at the edges are introduced by the neutralized solar wind.

ENA energy of 100 eV and a radial spacecraft velocity of 50 km s^{-1} (see Equation (12)), but this would not qualitatively affect the subsequent discussion.

The ribbon and GDF ENA sources, plasma cooling, and ENA losses outside the heliopause are included. The subsequent figures show hemispherical images of predicted ENA intensities for an observer looking back toward the heliosphere; all plots are centered on the Sun. The ENA maps around solar wind energy (1 keV ENAs) are dominated by the ENA ribbon and the very intense direct solar wind ENA emission close to the Sun.

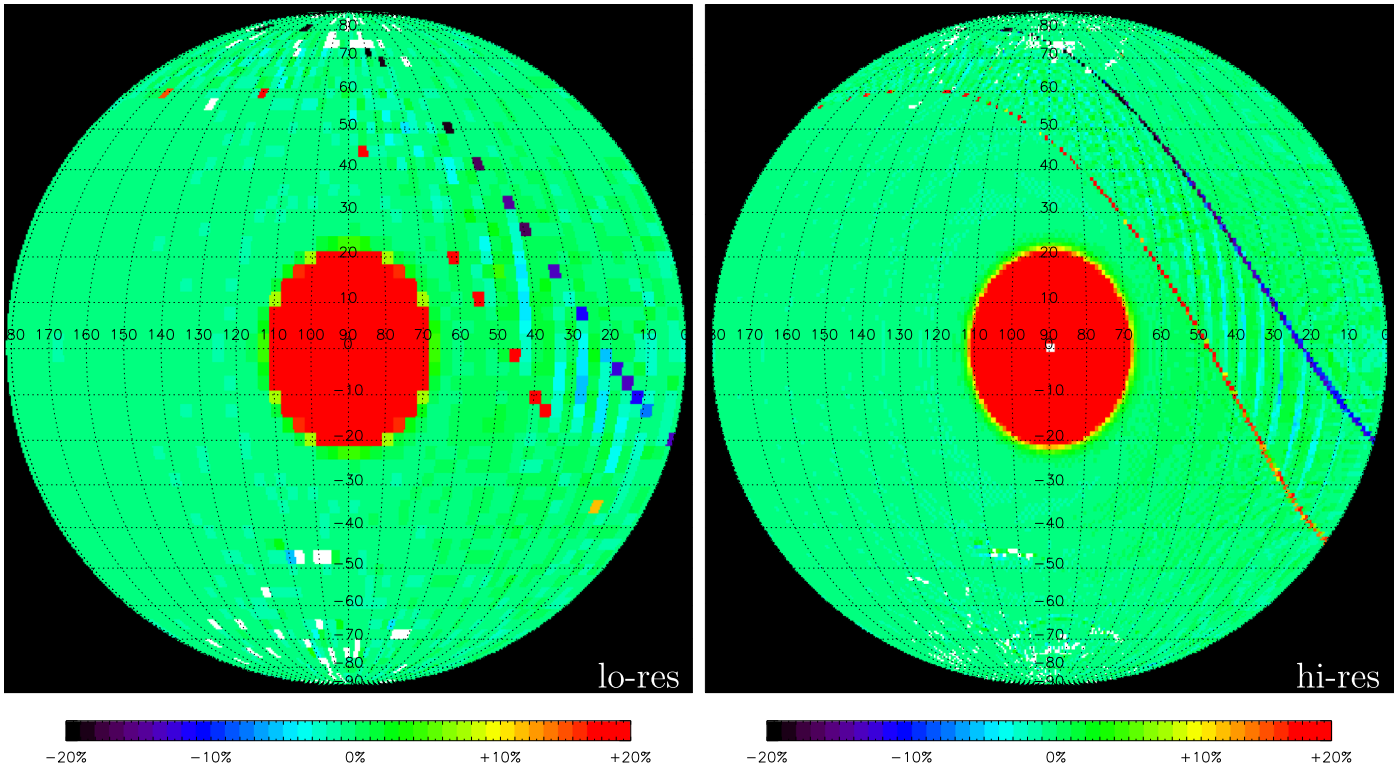

Figure 6. Relative differences in ENA intensities at 1 keV for the flank of the heliosphere (downwind direction at the left edge, upwind at the right edge of map) when observed with angular resolution = 3° × 3° (left panel) vs. high resolution of 1° × 1° (right panel). The observer vantage points used for these images are again the opposite positions at $\varphi = 90°$ and $\varphi = 270°$ for 2 au heliocentric distance.

3.2.1. Circular Orbits and Parallaxes

We created hemispherical ENA maps for an observer close to the ecliptic plane at $R = 2$, 3, 5, and 10 au on a circular orbit from $\varphi = 0°$, 90°, 180°, and 270° ($\varphi = 0°$ denoting the spacecraft position between the Sun and the nose of the heliosphere). The most instructive case is the comparison of the ENA maps of the upwind hemisphere as seen from $\varphi = 0°$ versus $\varphi = 180°$, or seen from flank positions $\varphi = 90°$ versus $\varphi = 270°$. We always assumed the large ellipsoid as heliosphere shape here, as this makes detecting parallax effects more difficult. The default angular resolution of the maps was 3° × 3° (see Section 3.1.3). We then calculated the relative differences in ENA intensity from the maps obtained at opposite positions around the Sun. As motivated in Section 3.1.2, we searched for pixels revealing a relative difference in predicted ENA intensity of at least 10%. We concentrated on 1 keV ENA energy to study the parallax effects both for the GDF and for the ENA ribbon. The disadvantage of this energy is the direct solar wind signal (and in reality also the solar UV) blotting out the part of the maps within 20° to the Sun direction.

We found that the parallax of the ribbon induces a 10% change in ≫10 pixels in upwind hemisphere maps if an observer baseline of 2 × 3 au or longer is assumed. A baseline of at least 2 × 5 au is required if the downwind hemisphere is considered instead. This holds true both for a comparison between upwind and downwind position ($\varphi = 180°$ and $\varphi = 0°$) and for a comparison between the flank positions at $\varphi = 90°$ and $\varphi = 270°$. Figure 5 shows the relative ENA differences in the upwind hemisphere as seen from a circular orbit at heliocentric distances increasing from 2 au (top left) to 10 au (bottom right). For this series of plots, the maps from vantage points $\varphi = 90°$ and $\varphi = 270°$ were subtracted from each other. A baseline of 2 × 2 au, on the other hand, is only sufficient to spot the systematic parallax pattern of the ribbon if the ENA image is acquired at a 1° × 1° degree resolution. This is illustrated by the comparison in Figure 6.

Apart from the ribbon, parallax effects of the GDF can also be used—in a much wider energy range—to determine the dimensions of the inner heliosheath. A baseline of roughly 2 × 10 au is required for systematic differences of 10% to appear in the GDF toward the nose of the heliosphere (bottom right panel of Figure 5). The relative differences in ENA intensities seen toward the flanks and poles also exceed the 10% limit for a baseline of 2 × 10 au. These differences in apparent GDF intensities are demonstrated in Figure 7: it shows the differences of two ENA maps of the downwind hemisphere observed from upwind and downwind positions $\varphi = 0°$ and $\varphi = 180°$, 10 au away from the Sun. This figure also shows that the GDF ENA intensity from the vast area within 70° around the downwind direction does not change by more than a few percent for a baseline of 2 × 10 au. This holds true for any other combination of vantage points on an orbit at 10 au heliocentric distance. Even for the case of the small ellipsoid heliopause, the parallax effects on ENA intensities are nondetectable toward downwind. This implies that the heliosheath dimensions in the downwind direction can only be determined directly by ENA imaging if a spacecraft goes for heliocentric distances well beyond Saturn.

3.2.2. Escape Orbits

The optimum trajectory of a future interstellar ENA imager must reach a compromise between reaching the heliopause

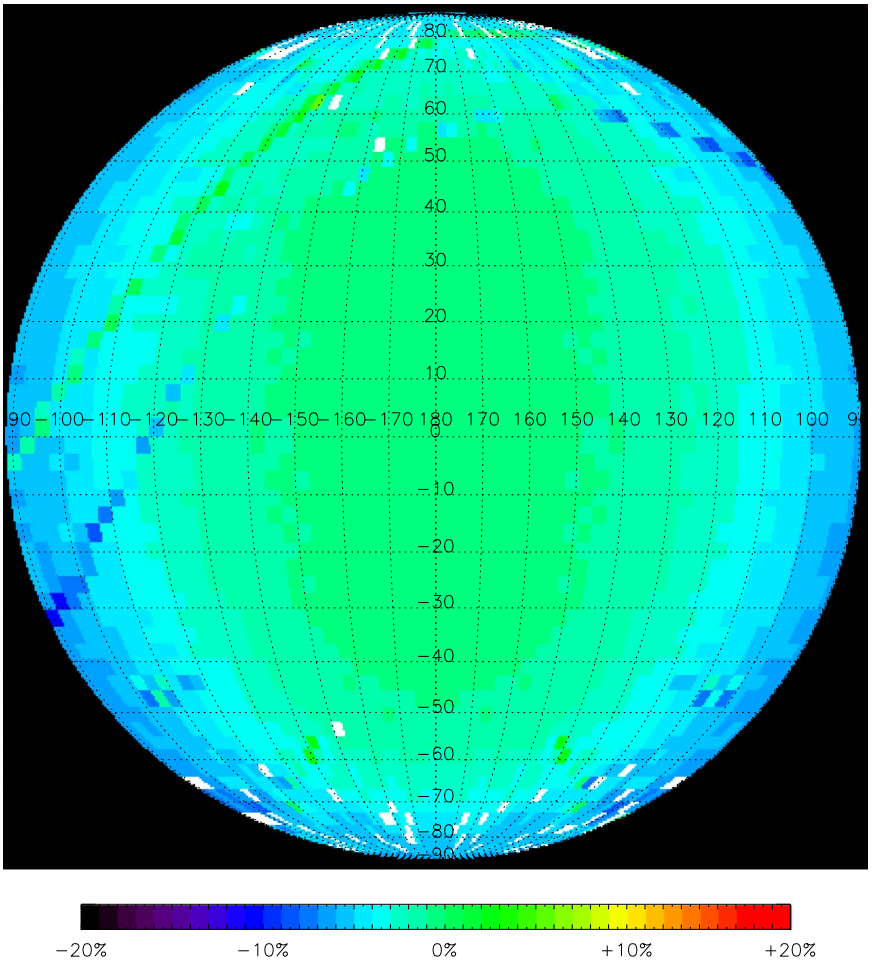

Figure 7. ENA map predictions for the relative differences in ENA intensities for the downwind hemisphere observed at 100 eV with angular resolution $= 3° \times 3°$ from vantage points at upwind and downwind positions ($\varphi = 0°$ vs. $\varphi = 180°$) at 10 au heliocentric distance.

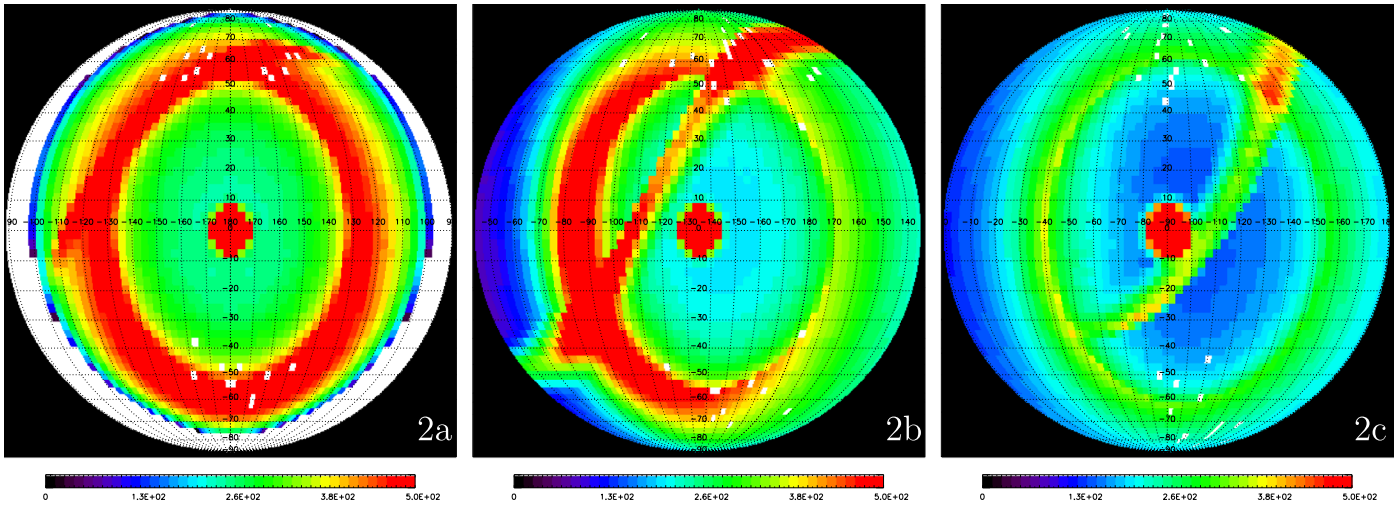

Figure 8. Effect of offset between viewing angle and ribbon center, with ENA intensities predicted for a heliocentric distance of 120 au at 1 keV for a large ellipsoid heliosphere. Left: observer placed in front the nose of the heliosphere (trajectory 2a: $\varphi = 0°$, $\vartheta = 0°$); middle: observer placed at (trajectory 2b: $\varphi = 45°$, $\vartheta = 0°$). Right: observer placed in the flank of the heliosheath with a 90° angle between the Sun–spacecraft and the Sun–upstream line (trajectory 2c: $\varphi = 90°$, $\vartheta = 0°$).

within a reasonable time, imaging the hitherto-unknown downwind regions, and being able to separate the ribbon ENAs from the GDF from the heliosheath. The trajectory should offer viewing angles rather perpendicular to both the symmetry axis of the heliosphere and the Sun–ribbon center line. For some longitudes, the maximum ribbon ENA emissions will strongly overlap with those from the GDF around the plasma boundaries, which would complicate interpretation of both ENA sources. This is illustrated by the comparison of the ENA maps (Figure 8) predicted for trajectories 2a, 2b, and 2c (from left to right) for

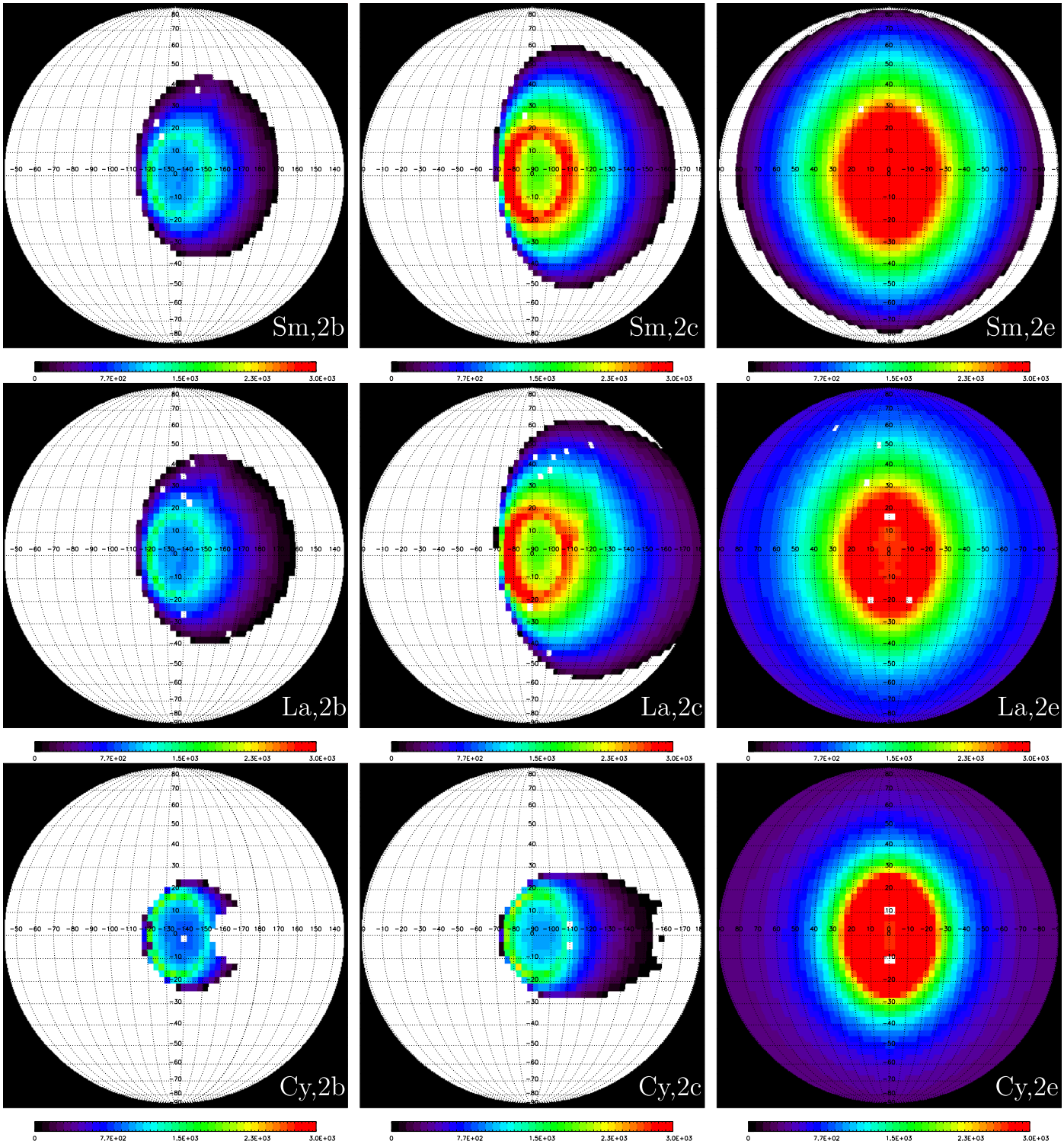

Figure 9. ENA map predictions at 400 au heliocentric distance for different heliospheric shapes and vantage points for 100 eV ENA energy. Columns from left to right: intermediate between nose and flank (2b), flank (2c), and downwind observer position (2e); rows from top to bottom: small ellipsoid, large ellipsoid, and cylindrical shape for heliopause. The Sun is always in the map center, and the color scale is identical across all plots (red pixels designate ENA intensities $j \geqslant 3000\ \mathrm{cm}^{-2}\ \mathrm{sr}^{-1}\ \mathrm{s}^{-1}\ \mathrm{keV}^{-1}$).

120 au heliocentric distance and 1 keV ENA energy. Trajectory 2a means heading directly toward the nose ($\lambda \approx 256°$, $\beta \approx 5°$ in ecliptic coordinates), Trajectory 2b corresponds to a path toward the ribbon region close to the ecliptic plane ($\lambda \approx 301°$), halfway between nose and flank on the port side of the heliosphere, with a 45° offset to the upwind direction and 81° to the ribbon center. Trajectory 2c implies the flank on the port side ($\lambda \approx 346°$), 90° away from the nose of the heliosphere.

Figure 9 illustrates an advantage for an ENA imager of following a flank trajectory (2c, middle column) compared to a rather noseward (2b, left column) or tailward direction (2e, right column) as seen from 400 au heliocentric distance and an

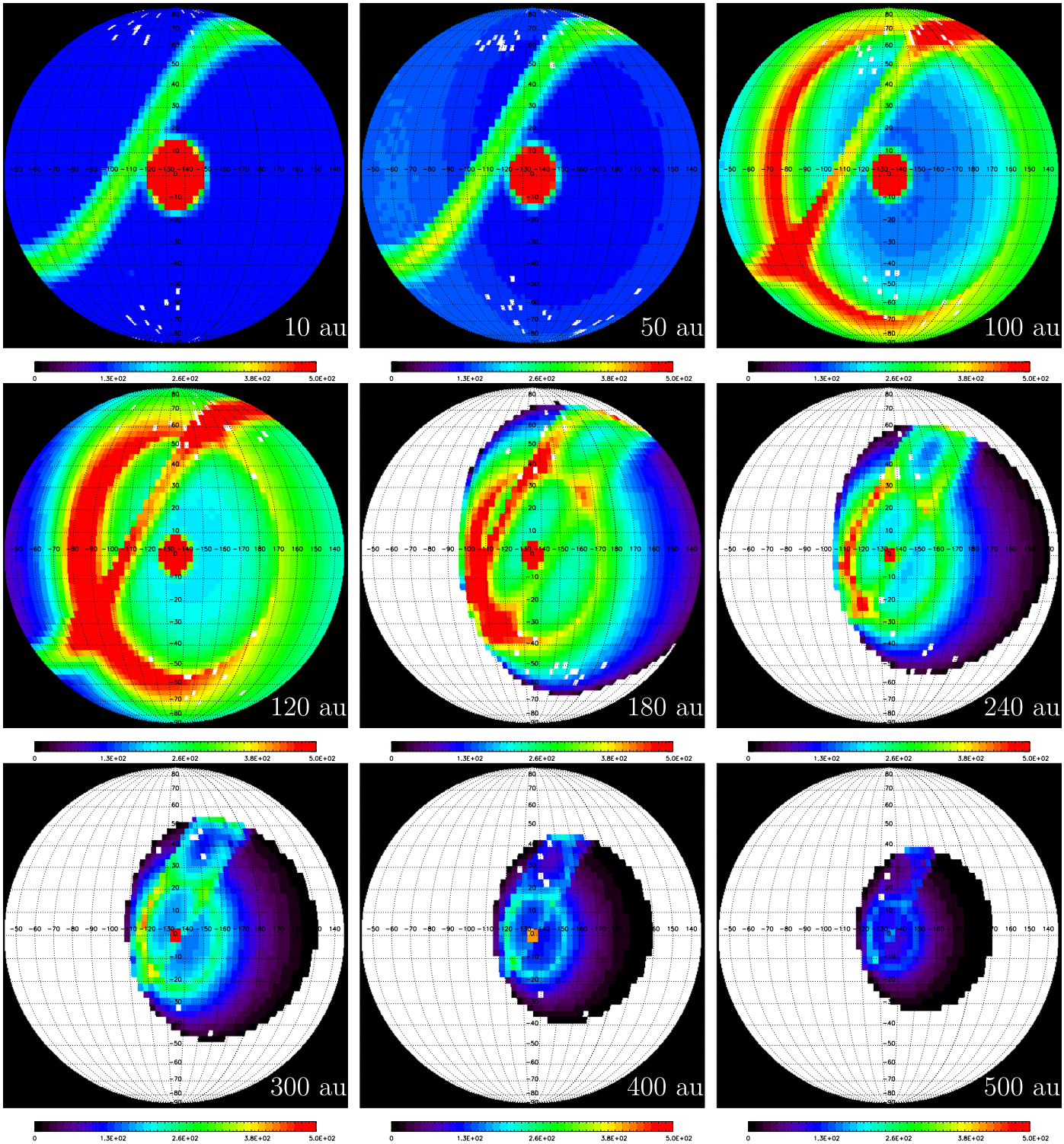

Figure 10. Map predictions for 1 keV ENAs for a spacecraft moving radially outward at a 45° angle with respect to the nose region (2b), from heliocentric distances 10 to 500 au. The heliospheric shape assumed here is the large ellipsoid, and the color scale for ENA intensity is identical across all plots (red pixels designate ENA intensities $j \geqslant 500\ \mathrm{cm^{-2}\ sr^{-1}\ s^{-1}\ keV^{-1}}$).

ENA energy of 100 eV. Black pixels designate nondetectable ENA intensities ($j < 10\ \mathrm{cm^{-2}\ sr^{-1}\ s^{-1}\ keV^{-1}}$ in middle column); the interstellar ENA background was not modeled and therefore appears white in all plots. Different heliospheric shapes, such as the small ellipsoid (top row), large ellipsoid (middle row), and Parker shape (bottom row), are best distinguished when observed from the flank (middle column). The mean free path length for 100 eV protons in the heliosheath is sufficient to make ENAs of the same energy a useful tracer to image the full extent of the heliopause. The same holds true for ENAs with energies much higher than 10 keV. However, for a downwind trajectory (case 2e, $\varphi = 180°$, $\vartheta = 0°$; left column in Figure 9) even such basic differences in heliosphere shape would be difficult to spot. In

addition, 400 au distance toward the downwind direction would not even be sufficient to cross the heliopause even if the real heliosphere resembles the small ellipsoid. A trajectory toward the nose obviously does not share this drawback, but some different heliosphere shapes are impossible to distinguish from the helionose (scenario 2a) and may still be difficult to distinguish for 2b (see top left versus middle left panels in Figure 9).

From Figures 8 and 9, trajectories similar to 2b or 2c appear to offer the most rewarding vantage points for ENA imaging of the heliosphere. Trajectory 2b would also offer the opportunity to sample the plasma populations of the ribbon region in situ but has less of a novelty value because it is closer to the trajectories of *Voyager 1* and *2*. Moreover, the heliosphere to the nose direction can be constrained more easily than any other region with ENA observations from the inner solar system (see previous section). Trajectory 2c would offer a better look at the vast downwind regions of the heliosphere in ENA emissions, but reaching the heliopause would take longer and ISN measurements would become more difficult compared to 2b.

Leaving the ecliptic plane (tested for trajectory 2d with $\vartheta = 30°$) changes the apparent position of the ribbon and the plasma boundaries. However, these predicted ENA images do not sufficiently differ from the images closer to the ecliptic at the same longitude to justify the effort of reaching higher ecliptic latitudes and the potential loss of science opportunities related to Kuiper Belt objects close to the ecliptic plane.

We finish this section by showing a series of consecutive ENA maps for 1 keV (Figure 10) predicted for a spacecraft leaving the solar system toward the flank of the heliosphere (trajectory 2b, $\varphi = 45°$, $\vartheta = 0°$). The ENA imager is looking back to the Sun while measuring ENAs of 1 keV energy. The heliocentric distances increase from top left to bottom right (10, 50, 100, 120, 180, 240, 300, 400, and 500 au), and the assumed heliosphere shape is the large ellipsoid. Passing through the termination shock (roughly at 90 au for this trajectory) dramatically changes the ENA map. The ribbon and the neutralized solar wind are prominent features at 1 keV from near and far, and the GDF from the heliosheath indicates the full dimensions of the heliosphere. Because of the short plasma cooling length for protons of 1–10 keV in the heliosheath, the farther reaches of the heliosheath in the downwind direction are difficult to image at intermediate energy, but these regions will be visible at lower or higher ENA energies.

4. Conclusions

We have designed a simple empirical model of heliospheric protons and neutral hydrogen to predict images of ENA intensities for a virtual observer inside or outside the heliosphere. The proton distributions are scaled so as to reproduce the known heliospheric ENA intensities observed close to 1 au. The neutral hydrogen is modeled as a static density; trajectories of ISNs throughout the heliosphere are not included yet. We chose this empirical approach to be able to easily visualize geometrical effects on heliospheric ENAs for any virtual position and for various heliosphere shapes.

Based on this empirical model and our experience from previous heliospheric ENA imaging missions, some general recommendations for angular resolution and sensitivity of ENA instrumentation have been derived. All ENA energies from 10 eV to 100 keV have their own merits to characterize the heliospheric plasma. This wide energy range necessitates two to three different ENA instruments. Given the uncertainties about the low-energy end of the heliospheric ENA spectrum and its relevance for heliosheath properties, a new heliosphere mission should attempt to image ENAs down to 10 eV.

For an ENA instrument on a spacecraft orbiting the Sun, the heliocentric distance should be at least 3 au to make use of parallax effects. For an ENA instrument on an interstellar probe, a radial escape trajectory through the flank regions of the heliosphere is preferable to the central upwind or central downwind direction to image the global shape of the heliosphere.

A.G. and P.W. acknowledge support from the Swiss National Science Foundation; H.F. acknowledges support on ENA-related research via DFG grant FI 706/21-1.

ORCID iDs

A. Galli https://orcid.org/0000-0003-2425-3793
P. Wurz https://orcid.org/0000-0002-2603-1169
H. Fichtner https://orcid.org/0000-0002-9151-5127

References

Barabash, S., Lundin, R., Andersson, H., et al. 2006, SSRv, 126, 113
Barabash, S., Sauvaud, J.-A., Gunell, H., et al. 2007, P&SS, 55, 1772
Barabash, S., Srama, R., Wieser, M., Wurz, P. & the LIMO Team 2019, in Local Interstellar Medium Observatory (LIMO): A Mission to Explore our Galactic Neighborhood (Vienna, Austria)
Barnett, C. F. 1990, Collisions of H, H_2, He and Li Atoms and Ions with Atoms and Molecules, Atomic Data for Fusion, Vol. 1, Oak Ridge National Laboratory, Report ORNL-6086
Brandt, P. C., McNutt, R. L., Paul, M. V., et al. 2019, JBIS, submitted
Burlaga, L. F., Ness, N. F., Acuña, M. H., et al. 2005, Sci, 309, 2027
Burlaga, L. F., Ness, N. F., Acuña, M. H., et al. 2008, Natur, 454, 75
Bzowski, M. 2008, A&A, 488, 1057
Bzowski, M., Sokół, J. M., Kubiak, M. A., & Kucharek, H. 2013, A&A, 557, A50
Dayeh, M. A., Zirnstein, E. J., Desai, M. I., et al. 2019, ApJ, 879, 84
DeMajistre, R., Brandt, P. C., & Roelof, E. C. 2018, in 42nd COSPAR Scientific Assembly (Pasadena, CA), PIR.1-27-18
Desai, M. I., Dayeh, M. A., Allegrini, F., et al. 2019, ApJ, 875, 91
Dialynas, K., Krimigis, S. M., Mitchell, D. G., Decker, R. B., & Roelof, E. C. 2017, NatAs, 1, 115
Elliott, H. A., McComas, D. J., Valek, P., et al. 2016, ApJS, 223, 19
Fahr, H. J., Fichtner, H., & Scherer, K. 2007, RvGeo, 45, RG4003
Fahr, H. J., Neutsch, W., Grzedzielski, S., Macek, W., & Ratkiewicz-Landowska, R. 1986, SSRv, 43, 329
Funsten, H. O., Allegrini, F., Bochsler, P., et al. 2009, SSRv, 146, 75
Fuselier, S. A., Allegrini, F., Bzowski, M., et al. 2012, ApJ, 754, 14
Fuselier, S. A., Allegrini, F., Bzowski, M., et al. 2014, ApJ, 784, 89
Fuselier, S. A., Bochsler, P., Chornay, D., et al. 2009, SSRv, 146, 117
Fuselier, S. A., Dayeh, M. A., & Möbius, E. 2018, ApJ, 861, 109
Fuselier, S. A., & Pope, S. 2005, Interstellar Boundary EXplorer (IBEX) Noise and Background Document, SwRI Proj.11343, Doc. No. 11343-IBEX BKGND-01
Futaana, Y., Barabash, S., Grigoriev, A., et al. 2006, Icar, 182, 413
Galli, A., Wurz, P., Fuselier, S. A., et al. 2014, ApJ, 796, 9
Galli, A., Wurz, P., Kollmann, P., et al. 2013, ApJ, 775, 24
Galli, A., Wurz, P., Rahmanifard, F., et al. 2019, ApJ, 871, 52
Galli, A., Wurz, P., Schwadron, N. A., et al. 2016, ApJ, 821, 107
Galli, A., Wurz, P., Schwadron, N. A., et al. 2017, ApJ, 851, 2
Giacalone, J., & Jokipii, J. R. 2015, ApJL, 812, 1
Gloeckler, G., & Fisk, L. A. 2011, in AIP Conf. Proc. 1302, Pickup Ions throughout the Heliosphere and Beyond, ed. J. A. Le Roux et al. (Melville, NY: AIP), 110
Gloeckler, G., & Fisk, L. A. 2015, ApJL, 806, L27
Gloeckler, G., & Geiss, J. 2001, in AIP Conf. Proc. 598, Solar and Galactic Composition: A Joint SOHO/ACE Workshop (Melville, NY: AIP), 281
Gosling, J. T. 2007, in Encyclopedia of the Solar System, ed. L. A. McFadden, P. R. Weissman, & T. V. Johnson (2nd ed.; San Diego, CA: Academic), 99

Gruntman, M., Roelof, E. C., Mitchell, D. G., et al. 2001, JGR, 106, 15767
Heerikhuisen, J., Zirnstein, E. J., Funsten, H. O., Pogorelov, N. V., & Zank, G. P. 2014, ApJ, 784, 73
Hilchenbach, M., Hsieh, K. C., Hovestadt, D., et al. 1998, ApJ, 503, 916
Ipavich, F. M. 1974, GeoRL, 1, 149
Izmodenov, V. V., & Alexashov, D. B. 2015, ApJS, 220, 32
Kallenbach, R., Hilchenbach, M., Chalov, S. V., Le Roux, J. A., & Bamert, K. 2005, A&A, 439, 1
Khabarova, O. V., Obridko, V. N., Kislov, R. A., et al. 2018, PlPhR, 44, 840
Krimigis, S. M., Mitchell, D. G., Roelof, E. C., Hsieh, K. C., & McComas, D. J. 2009, Sci, 326, 971
Kubiak, M. A., Bzowski, M., Sokół, J. M., et al. 2014, ApJS, 213, 29
Lindsay, B. G., & Stebbings, R. F. 2005, JGR, 110, A12213
Livadiotis, G., McComas, D. J., Schwadron, N. A., Funsten, H. O., & Fuselier, S. A. 2013, ApJ, 762, 134
Marsch, E., Mühlhäuser, K.-H., Schwenn, R., et al. 1982, JGR, 87, 52
McComas, D. J., Alexashov, D., Bzowski, M., et al. 2012, Sci, 336, 1291
McComas, D. J., Bzowski, M., Frisch, P., et al. 2010, JGR, 115, A09113
McComas, D. J., Bzowski, M., Fuselier, S. A., et al. 2015, ApJS, 220, 22
McComas, D. J., Christian, E. R., Schwadron, N. A., et al. 2018, SSRv, 214, 116
McComas, D. J., Dayeh, M. A., Funsten, H. O., et al. 2019, ApJ, 872, 127
McComas, D. J., Lewis, W. S., & Schwadron, N. A. 2014, RvGeo, 52, 118
McComas, D. J., Zirnstein, E. J., Bzowski, M., et al. 2017, ApJS, 229, 41
McNutt, R. L., Wimmer-Schweingruber, R. F., Gruntman, M., et al. 2018, ACAcu, 162, 284
Möbius, E., Bochsler, P., Bzowski, M., et al. 2012, ApJS, 198, 11
Müller, H.-R., & Zank, G. P. 2004, JGRA, 109, A07104
Opher, M. 2016, SSRv, 200, 475
Opher, M., Drake, J. F., Zieger, B., Swisdak, M., & Toth, G. 2016, PhPl, 23, 056501
Park, J., Kucharek, H., Möbius, E., et al. 2016, ApJ, 833, 130
Parker, E. N. 1961, ApJ, 134, 20
Pogorelov, N. V., Fichtner, H., Czechowski, A., et al. 2017, SSRv, 212, 193
Rahmanifard, F., Möbius, E., Schwadron, N. A., et al. 2019, ApJ, submitted
Reisenfeld, D. B., Bzowski, M., Funsten, H. O., et al. 2016, ApJ, 833, 277
Reisenfeld, D. B., Bzowski, M., Funsten, H. O., et al. 2019, ApJ, 879, 1
Rodríguez Moreno, D. F., Saul, L., Wurz, P., et al. 2012, P&SS, 60, 297
Roelof, E. C., Keath, E. P., & Bostrom, C. O. 1976, JGR, 81, 2304
Roelof, E. C., Mitchell, D. G., & Williams, D. J. 1985, JGR, 90, 10991
Röken, C., Kleimann, J., & Fichtner, H. 2015, ApJ, 805, 173
Saul, L., Wurz, P., Rodríguez, D., et al. 2012, ApJS, 198, 14
Scherer, K., & Fichtner, H. 2014, ApJ, 782, 25
Schwadron, N. A., Allegrini, F., Bzowski, M., et al. 2011, ApJ, 731, 56
Schwadron, N. A., & Bzowski, M. 2018, ApJ, 862, 11
Schwadron, N. A., Möbius, E., Fuselier, S. A., et al. 2014, ApJ, 215, 13
Stone, E. C., Cummings, A. C., McDonald, F. B., et al. 2013, Sci, 341, 150
Swaczyna, P., Bzowski, M., Christian, E. R., et al. 2016, ApJ, 823, 119
Swaczyna, P., Grzedzielski, S., & Bzowski, M. 2017, ApJ, 840, 75
Sylla, A., & Fichtner, H. 2015, ApJ, 811, 150
Witte, M. 2004, A&A, 426, 835
Wurz, P. 2000, in The Outer Heliosphere: Beyond the Planets, ed. K. Scherer, H. Fichtner, & E. Marsch (Katlenburg-Lindau: Copernicus Gesellschaft e.V.), 251
Wurz, P., Fuselier, S. A., Möbius, E., et al. 2009, SSRv, 146, 173
Zank, G. P., Heerikhuisen, J., Wood, B. E., et al. 2013, ApJ, 763, 20
Zirnstein, E. J., Funsten, H. O., Heerikhuisen, J., & McComas, D. J. 2016a, A&A, 586, A31
Zirnstein, E. J., Funsten, H. O., Heerikhuisen, J., et al. 2016b, ApJ, 826, 58
Zirnstein, E. J., Giacalone, J., Kumar, R., et al. 2019, ApJ, submitted
Zirnstein, E. J., Kumar, R., Heerikhuisen, J., McComas, D. J., & Galli, A. 2018, ApJ, 860, 170
Zong, Q.-G. 2018, in 42nd COSPAR Scientific Assembly (Pasadena, CA), PIR.1-2-18